Received April 29, 2021, accepted May 18, 2021, date of publication May 24, 2021, date of current version June 8, 2021.

*Digital Object Identifier 10.1109/ACCESS.2021.3083100*

# Optimization of *LLC* Resonant Converter With Two Degrees of Freedom Based on Operation Stage Trajectory Analysis

**ZIHENG XIAO[1,2], (Student Member, IEEE), ZHIXING HE[1,2], (Member, IEEE), YONG NING[2], HONGLIANG WANG[1,2], (Senior Member, IEEE), AN LUO[1,2], (Senior Member, IEEE), YANDONG CHEN[1,2], (Senior Member, IEEE), AND JUNLING CHEN[2]**

[1]Guangdong Zhicheng Champion Group Company Ltd., Dongguan 523718, China
[2]College of Electrical and Information Engineering, Hunan University, Changsha 410082, China

Corresponding author: Zhixing He (hezhixingmail@163.com)

This work was supported by the Program for Guangdong Introducing Innovative and Enterpreneurial Teams under Grant 2017ZT07G237.

**ABSTRACT** *LLC* resonant DC-DC converter has been widely used in high power density and high efficiency applications. Pulse frequency modulation (PFM) is commonly applied due to its wide soft-switching range. In some special cases, phase shift modulation (PSM) is applied to widen voltage regulation range, improve light-load efficiency, or implement a soft start-up process. Because *LLC* is with 2 control degrees of freedom (2DOFs), switching frequency and duty ratio, a unified analysis and optimization for *LLC* with 2DOFs is desired. This paper makes an effort to present a unified time domain operation stage trajectories (OSTs) analysis of *LLC*. On this basis, a unified numerical optimization method is proposed with arbitrarily designed optimization objectives. With the proposed optimization method, the optimized *LLC* with 2DOFs is with better performance compared to conventional PFM and PSM, which is verified by the experimental results.

**INDEX TERMS** LLC resonant converter, soft-switching, operation stage trajectory analysis, optimization.

## I. INTRODUCTION

The *LLC* resonant converter is a popular resonant converter widely used in server power supply [1]–[4], LED driver [5]–[7], electric vehicles (EV) [8]–[10], and renewable energy systems [11]–[13] with the advantage of wide voltage gain, galvanic isolation, high power and high power density. Besides, zero voltage turning-on (ZVS-on) for primary MOSFETs and zero current turning-off (ZVS-off) for secondary diodes can be achieved in wide input voltage and load range, making it suitable for high frequency conversion with high efficiency [14]–[16]. The topology of the *LLC* resonant converters are depicted in Fig. 1. $C_{DC1}$, and $C_{DC2}$ are two DC capacitors. $S_1$-$S_4$ are 4 MOSFETs for the full-bridge (FB) *LLC* resonant converter in Fig. 1(a). $S_1$ and $S_2$ are 2 MOSFETs for the half-bridge (FB) *LLC* resonant converter in Fig. 1(b). $D_1$-$D_4$ are 4 rectifier diodes. The turn ratio of the high frequency transformer (HFT) is 1: $n$ and the switching frequency is $f_s$. The resonant tank is formed by resonant capacitor $C_r$, resonant inductor $L_r$ and excitation inductor $L_m$, where $L_m = (m-1)\,L_r$, and $m$ is denoted as inductor ratio.

The associate editor coordinating the review of this manuscript and approving it for publication was Francisco Perez-Pinal.

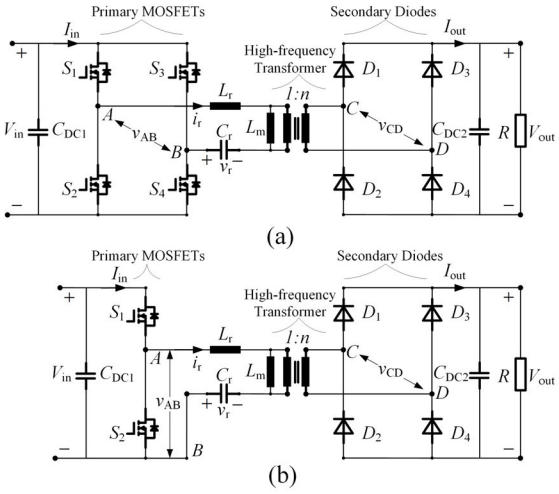


**FIGURE 1.** (a) Topology of FB *LLC* resonant converter.(b) Topology of HB *LLC* resonant converter.

The input voltage, input current, output voltage, and output current of the *LLC* are denoted as $V_{in}$, $I_{in}$, $V_{out}$, and $I_{out}$, respectively. The resonant current and resonant voltage are denoted as $i_r$, and $v_r$. The resonant frequency of $L_r$ and $C_r$

is denoted as series resonant frequency $f_r$ and the resonant frequency of $L_r$, $L_m$, and $C_r$ is denoted as series parallel resonant frequency $f_m$.

The *LLC* is a 2 control degrees of freedom (2DOF) system (switching frequency $f_s$ and duty-ratio $D$). Pulse frequency modulation (PFM) is widely applied due to wide voltage regulation and ZVS range where the duty-ratio $D$ is fixed to unity. PFM with predefined dead time control is presented in [16]–[18], PFM with trajectory control has been applied to *LLC* for soft-start [19], [20], burst mode [21], and light load efficiency improvement [6], [22]. Design and efficiency optimization of *LLC* with PFM were reported in [16], [23]–[26]. In PFM when $f_s$ moves away from $f_r$, the efficiency degrades rapidly [14], [15], [27]. Moreover, to achieve a low voltage gain, $f_s$ needs to be considerably higher than $f_r$, which adds to more switching loss. Additionally, to achieve a high voltage gain, $f_s$ needs to be lower than $f_r$. The lower bound of $f_s$ limits the size of the transformer and the power density of *LLC*. Some new applications require *LLC* to operate over extremely wide voltage gain and load range, which cannot be practically provided just with PFM. When $f_s$ is fixed to $f_r$ and only $D$ is regulated, the modulation is denoted as the phase shift modulation (PSM). With PSM, the equivalent input voltage is reduced and the voltage regulation range is extended [28]–[30]. Besides, PSM has also been used to suppress in-rush current during the start-up process [31], [32]. The above articles provide some control algorithms to enhance the efficiency or power density of *LLC*, but the 2DOFs are usually analyzed separately. Because there is only one control variable while the other is fixed, only local optimization can be obtained.

The analysis methods of *LLC* can be divided into three approaches: frequency domain analysis, frequency domain analysis with time domain correction, and time domain analysis. In frequency domain analysis, fundamental harmonic approximation (FHA) [16], [23], [33] is widely used due to its simple concept. FHA shows good accuracy when $f_s$ is close to $f_r$. However, the accuracy degrades when $f_s$ moves away from $f_r$. When FHA is adopted to PSM, significant errors occur in the estimation of electric quantities and key circuit parameters [34]. As for frequency domain analysis with time domain correction, enhanced FHA (eHFA) considers the phase lag of resonant current and voltage, and the equivalent AC resistance is regarded as a complex impedance [35]. However, the accuracy degrades in discontinuous current mode (where $I_{out}$ is discontinuous). [36] made an adjustment of the load factor and the error is compensated. However, there are still some errors between theoretical results and practical results in some operation points, which leads problems in the design of *LLC*. In time domain analysis, according to different resonant conditions in one switching cycle, *LLC* can be divided into several stages and the operation of *LLC* can be summarized as different operation stage trajectories (OSTs). In PFM, the operation modes of the *LLC* are classified into three types in [37]. An optimal design procedure for *LLC* is presented in [25]. In PSM, operation modes are further classified in [38], but no specific solution is given. An analytical model has been proposed in [39], but not all possible modes are applicable. A multimode optimization of *LLC* in PSM is discussed in [31]. In short, most literature only focuses on PFM or PSM, and the comparison is not comprehensive since there is only one DOF in PFM or PSM.

This paper makes an effort to present a unified time domain OST analysis for *LLC* with 2DOFs. On this basis, the *LLC* is optimized from the following perspective:

1) Wide voltage and load regulation range.
2) Narrow switching frequency regulation range.
3) Low values of electric quantities ($I_{RMS}$, $I_{mRMS}$, $I_{Peak}$, $V_{Peak}$).
4) ZVS-on for MOSFETs and ZCS-off for diodes should be achieved when the *LLC* operates with wide input and output voltage range.

This paper is further organized as follows. Operation stages and OSTs are introduced in Section II. The OSTs and distribution in PFM and PSM is presented in Section III. Steady-state parameter estimation of *LLC* is summarized in Section IV. The optimization of *LLC* with 2DOFs is presented in Section V. Then the experimental results are presented in Section VI, and the conclusions are drawn in Section VII.

## II. OPERATION STAGE TRAJECTORY ANALYSIS OF LLC

### A. OPERATION STAGES OF LLC

To simplify the analysis, normalized variables are used. The normalized analysis is both suitable for FB and HB *LLC* and the following analysis will take FB *LLC* for example. The frequency base $f_{Base}$, duration base $\theta_{Base}$, voltage base $V_{Base}$, impedance base $Z_{Base}$, current base $I_{Base}$, power base $P_{Base}$, quality factor $Q$, and voltage gain $M$ are given as

$$f_{Base} = f_r = \frac{1}{2\pi\sqrt{L_r C_r}}, \theta_{Base} = 2\pi f_r t, V_{Base} = \frac{V_{out}}{n},$$
$$Z_{Base} = Z_r = \sqrt{\frac{L_r}{C_r}}, I_{Base} = \frac{nZ_r}{V_{out}}, P_{Base} = \frac{V_{out}^2}{n^2 Z_r},$$
$$Q = \frac{\pi^2 n^2 Z_r}{8R}, M = \frac{V_{out}}{nV_{in}}. \quad (1)$$

The variables after normalization are represented by the corresponding capital letters.

The full order and the lossless model of the *LLC* are depicted in Fig. 2. As for the full order model, the magnetizing inductance, magnetizing resistance, winding inductance, and winding resistance in the primary side and secondary side are denoted as $L_M$, $R_M$, $L_{tr1}$, $L_{tr2}$, $R_{tr1}$, and $R_{tr2}$, respectively. As for the lossless model, the core loss and copper loss are assumed to be zero. Hence, $L_M$ and $R_M$ are infinity and $R_{tr1}$ and $R_{tr2}$ are zero.

The input voltage of resonant tank $V_{AB}$ can be $1/M$, 0, or $-1/M$. The equivalent output voltage of resonant tank $V'_{CD}$ can be 1, or $-1$. $S_0$ is the equivalent switch for secondary diodes. When $S_0 = 1$, $V'_{CD} = 1$, diodes $D_1$ and $D_4$ conduct; When $S_0 = 1$, $V'_{CD} = -1$, diodes $D_2$ and $D_3$ conduct; When $S_0 = 0$, four diodes are cutoff.

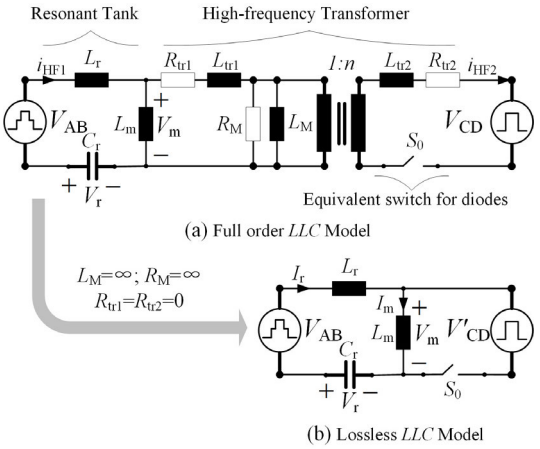


**FIGURE 2.** Model of *LLC* resonant converter. (a) Full order model. (b) Lossless model.

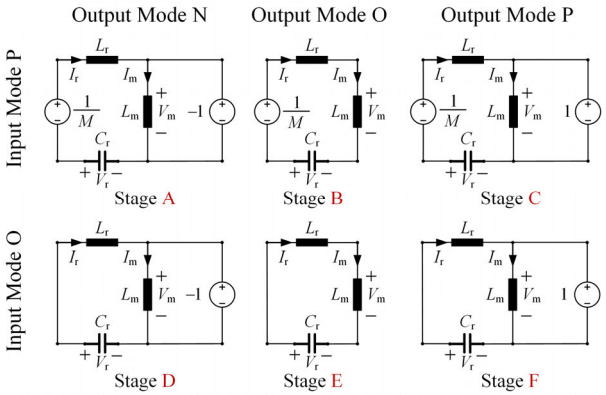


**FIGURE 3.** 6 possible stages in half switching cycle.

According to the value of $V_{AB}$, $V'_{CD}$, and $S_0$, the operation of *LLC* can be classified into nine stages. Due to the half-wave symmetry (HWS) characteristic of resonant waveforms, only six stages named from stage A to stage F need to be considered in half switching cycle. The 6 possible stages are depicted in Fig. 3.

$I_{rX}(\theta)$, $I_{mX}(\theta)$, $V_{rX}(\theta)$, and $V_{mX}(\theta)$ denotes the normalized resonant current, excitation current, resonant voltage, and excitation voltage, where $X$ = A, B, C, D, E, and F. Due to the characteristic of resonant tank, $I_{rX}(\theta)$, $I_{mX}(\theta)$, $V_{rX}(\theta)$, and $V_{mX}(\theta)$ can be decomposed into sine terms, cosine terms, and DC terms.

Because the input and output of the *LLC* resonant tank are both voltage sources, $I_{rX}(\theta)$ is without DC terms, and the DC terms of $V_{rX}(\theta)$ is determined by $V_{AB}$ and $V'_{CD}$ in different stages. As for output mode P/N, $L_m$ is positively/negatively clamped by the output voltage. Hence, $V_{mX}(\theta)$ equals $-1/1$, and $I_{mX}(\theta)$ increases/decreases linearly from the initial value with the slope $1/(m-1)$.

Hence, steady state equations in stage A are given as

$$\begin{cases} I_{rA}(\theta) = \left(1 + \dfrac{1}{M} - V_{rA}(0)\right)\sin(\theta) + I_{rA}(0)\cos(\theta) \\ I_{mA}(\theta) = I_{mA}(0) - \dfrac{\theta}{m-1} \\ V_{rA}(\theta) = \left(1 + \dfrac{1}{M}\right) - \left(1 + \dfrac{1}{M} - V_{rA}(0)\right) \\ \qquad \cos(\theta) + I_{rA}(0)\sin(\theta) \\ V_{mA}(\theta) = -1 \end{cases} \tag{2}$$

Output mode O is quite different as $L_m$ joins the resonance and the resonant frequency changed from $F_r$ to $F_m$. In output mode O, there is $I_{rX}(\theta) = I_{mX}(\theta)$. $V_{mX}(\theta)$ is calculated by voltage division law, which is between $-1$ and 1 to prevent the conduction of diodes.

Hence, steady state equations in stage B are given as

$$\begin{cases} I_{rB}(\theta) = I_{mB}(\theta) = \dfrac{\sqrt{m}}{m}\left(\dfrac{1}{M} - V_{rB}(0)\right) \\ \sin\left(\dfrac{\theta}{\sqrt{m}}\right) + I_{rB}(0)\cos\left(\dfrac{\theta}{\sqrt{m}}\right) \\ V_{rB}(\theta) = \dfrac{1}{M} - \left(\dfrac{1}{M} - V_{rB}(0)\right)\cos\left(\dfrac{\theta}{\sqrt{m}}\right) \\ +\sqrt{m}I_{rB}(0)\sin\left(\dfrac{\theta}{\sqrt{m}}\right) \\ V_{mB}(\theta) = \dfrac{m-1}{m}\left(\dfrac{1}{M} - V_{rB}(0)\right)\cos\left(\dfrac{\theta}{\sqrt{m}}\right) \\ -\dfrac{m-1}{\sqrt{m}}I_{rB}(0)\sin\left(\dfrac{\theta}{\sqrt{m}}\right) \end{cases} \tag{3}$$

Steady state equations in stage C to stage F are given in the appendix.

### B. OPERATION STAGE TRAJECTORIES OF LLC

Different combinations of stages in half switching cycle form the OST. For example, C-FE indicates that the resonant tank first operates in stage C and then enters stage F and finally enters stage E. A hyphen is used to denote the transition from $V_{AB} = 1/M$ to $V_{AB} = 0$. Because the OST combines different stages, the boundary of adjacent stages needs to be analyzed. If we use $X$, $Y$ to denote two different adjacent modes, the continuity equations are given as

$$I_{rX}(\theta_X) = I_{rY}(0),\ I_{mX}(\theta_X) = I_{mY}(0),\ V_{rX}(\theta_X) = V_{rY}(0). \tag{4}$$

If $Y$ is the last stage in half switching cycle while $X$ is the first stage, the half wave symmetric (HWS) equations are given as

$$\begin{aligned} \text{FB}: -I_{rX}(0) &= I_{rY}(\theta_Y),\ -I_{mX}(0) = I_{mY}(\theta_Y), \\ -V_{rX}(0) &= V_{rY}(\theta_Y). \\ \text{HB}: I_{rX}(0) &= I_{rY}(\theta_Y),\ I_{mX}(0) = I_{mY}(\theta_Y), \\ V_{rX}(0) &= V_{rY}(\theta_Y). \end{aligned} \tag{5}$$

There are two kinds of stage transitions (i.e. the input mode transition and the output mode transition). The input mode transition is determined by MOSFETs, and the transition

condition is given as $\Sigma\theta + \theta_X = D\pi$ ($\Sigma\theta$ denotes the sum of stage durations before stage $X$). The output mode transition (A↔B, A↔C, B↔C, D↔E, D↔F, and E→F) is determined by diodes, and the transition condition is slightly complicated. When $X$ = A/C/D/F, the transition condition is given as $I_{mX}(\theta_X) = I_{rX}(\theta_X)$. When $X$ = B/E, the transition condition is given as $V_{mX}(\theta_X) = \pm 1$ (1 when $Y$ = C/F, $-1$ when $Y$ = A/D).

The detailed stage transition conditions is summarized in the Appendix for a better understanding.

The duration balance equation is given as

$$\begin{aligned}
&\text{FB:}\theta_A + \theta_B + \theta_C = \frac{D\pi}{F}, \theta_D + \theta_E + \theta_F = \frac{(1-D)\pi}{F}.\\
&\text{HB:}\theta_A + \theta_B + \theta_C = \frac{2D\pi}{F}, \theta_D + \theta_E + \theta_F = \frac{2(1-D)\pi}{F}.
\end{aligned} \tag{6}$$

Average input power $P_{in}$ and output power $P_{out}$ of a FB *LLC* are given as

$$\begin{aligned}
P_{in} = &\frac{F}{M\pi}\left(\int_0^{\theta_A} I_{rA}(\theta)d\theta + \int_0^{\theta_B} I_{rB}(\theta)d\theta\right.\\
&\left.+\int_0^{\theta_C} I_{rC}(\theta)d\theta\right),\\
P_{out} = &\frac{F}{\pi}\left(\int_0^{\theta_C} (I_{rC}(\theta) - I_{mC}(\theta))\,d\theta\right.\\
&\left.+\int_0^{\theta_F} (I_{rF}(\theta) - I_{mF}(\theta))\,d\theta\right)\\
&-\frac{F}{\pi}\left(\int_0^{\theta_A} (I_{rA}(\theta) - I_{mA}(\theta))\,d\theta\right.\\
&\left.+\int_0^{\theta_D} (I_{rD}(\theta) - I_{mD}(\theta))\,d\theta\right).
\end{aligned} \tag{7}$$

Assume there is no power loss during power conversion, the power balance equation is given as $P = P_{in} = P_{out} = 8Q/\pi^2$. As for a HB *LLC*, $P$ and $M$ are reduced by half.

As for an $N$-stage OST, although there are four variables ($I_{rX}(\theta)$, $I_{mX}(\theta)$, $V_{rX}(\theta)$, and $V_{mX}(\theta)$), only three of them are independent (stage A and stage D are with $V_m(\theta) = -1$, stage B and stage E are with $I_r(\theta) = I_m(\theta)$, stage C and stage F are with $V_m(\theta) = 1$). Hence, the number of unknowns for stage $X$ is four (three of the four variables, and duration $\theta_X$), and the total unknowns are $4N+1$ ($M$ is also unknown). The number of equations is also $4N+1$, which can be classified into $3(N-1)$ continuity equations, 3 HWS equations, $N-1$ transition equations, one duration balance equation, and one power balance equation. Because the transition equation of output mode P and O is transcendental, no analytical expressions can be given for OSTs with this type of boundary transition equation.

There are four conditions for one OST.

1) The start stage should be stage A, B, or C. The end stage should be stage D, E, or F.

2) Adjacent stages belong to the same input mode or the same output mode, e.g. the transition from stage A to stage E is prohibited.

3) OSTs should contain stage C.

4) The start stage and the end stage belong to two opposite output modes due to HWS conditions.

With these conditions, there are six possible OSTs, CBA-D, ABC-F, CB-ED, BC-FE, C-FED, and BCB-E. Other OSTs are just special cases of these OSTs. For instance, OST C-FE is a special case of BC-FE with $\theta_B = 0$. OSTs CBA-D and CB-ED only appear when $F < 1$, OST ABC-F only appears when $F > 1$. OSTs BCB-E and BC-FE are with relative low $Q$.

## III. OSTS AND OST DISTRIBUTIONS IN PFM AND PSM

This section presents the OSTs and distributions in PFM and PSM to be expended to 2DOFs in the following section.

### A. OSTS IN PFM

In PFM, the possible OSTs are ABC, CBA, and BCB. OST C exists when $F = 1$ and large $Q$. OST BC, ABC, and AC appear when $F > 1$, OST CB, CBA, and CA appear when $F < 1$, and OST BCB exists in all $F$ range when $Q$ is relatively small. Fig. 4 show the waveforms of these OSTs.

As for OST C, there is $F = 1, M = 1$. Negative $I_{rC}(0)$ indicates that ZVS-on for MOSFETs (red circle in Fig. 4(a)) can always be achieved independent of load. However, ZCS-off for diodes (purple triangular in Fig. 4(a)) cannot be achieved due to continuous diode conduction current in stage C. As for OST BCB, ZVS-on for MOSFETs as well as ZCS-off for diodes (green triangular in Fig. 4(b)) can be achieved due to discontinuous diode conduction current in stage B.

The expressions of OST C are given as

$$\begin{cases}
I_{rC}(\theta) = \dfrac{4Q}{\pi}\sin(\theta) - \dfrac{\pi}{2(m-1)}\cos(\theta)\\
I_{mC}(\theta) = -\dfrac{\pi}{2(m-1)} + \dfrac{\theta}{m-1}\\
V_{rC}(\theta) = -\dfrac{4Q}{\pi}\cos(\theta) - \dfrac{\pi}{2(m-1)}\sin(\theta)
\end{cases}. \tag{8}$$

When $Q$ is small, stage B may exist at the beginning and end of the half switching cycle. The boundary is related to the slope of $I_r(\theta)$ and $I_m(\theta)$. If stage B comes at the beginning, the boundary $Q$ of OST C and OST BC can be obtained with

$$\frac{dI_{rC}(\theta)}{d\theta}|_{\theta=0} = \frac{dI_{mC}(\theta)}{d\theta}|_{\theta=0} \Rightarrow Q_{min} = \frac{\pi}{4(m-1)}. \tag{9}$$

If stage B comes at the end, the boundary $Q$ of OST C and OST CB can be obtained with

$$\frac{dI_{rC}(\theta)}{d\theta}|_{\theta=\pi} = \frac{dI_{mC}(\theta)}{d\theta}|_{\theta=\pi} \Rightarrow Q_{min} = \frac{\pi}{4(m-1)}. \tag{10}$$

(9) and (10) imply that two stage B come and disappear simultaneously when $F = 1$.

When $F > 1$, the duration of half switching cycle is changed to $\pi/F < \pi$. OST BCB still exists in tiny $Q$, and the latter stage B disappears first with the increasing of $Q$,

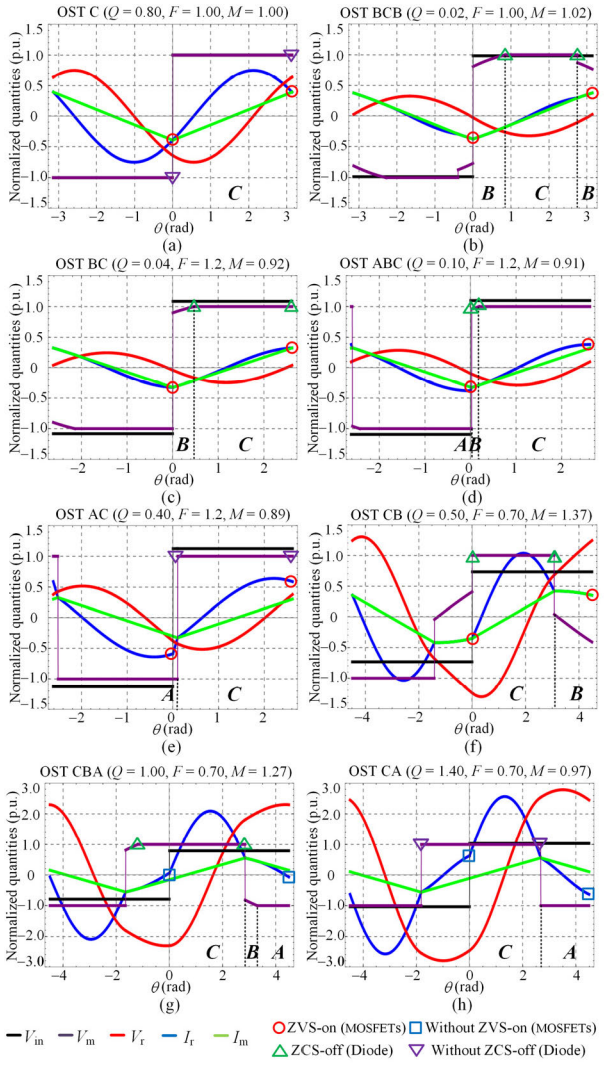


**FIGURE 4.** Typical waveforms in PFM. (a) OST C ($Q = 0.8$, $F = 1.0$, $M = 1.0$). (b) OST BCB ($Q = 0.02$, $F = 1.0$, $M = 1.02$). (c) OST BC ($Q = 0.04$, $F = 1.2$, $M = 0.9$). (d) OST ABC ($Q = 0.10$, $F = 1.2$, $M = 0.91$). (e) OST AC ($Q = 0.4$, $F = 1.2$, $M = 0.89$). (f) OST CB ($Q = 0.5$, $F = 0.7$, $M = 1.37$). (g) OST CB ($Q = 1.0$, $F = 0.7$, $M = 1.27$). (h) OST CA ($Q = 1.4$, $F = 0.7$, $M = 0.97$).

and the OST is changed to BC [see Fig. 4(c)]. Note that the mode transition equation is also the continuity equation in OST BC, which made OST BC a line in the OST distribution map in Fig. 7(a). When the latter stage B disappears, $I_r(\theta)$ is greater than $I_m(\theta)$ at the end of half switching cycle and the OST is ABC [see Fig. 4(d)]. When the initial slope of $I_r(\theta)$ is greater than that of $I_m(\theta)$ at the beginning of stage C, stage B disappeared and the OST is changed to AC [see Fig. 4(e)]. In summary, the OSTs when $F > 1$ are BCB, BC, ABC, and AC with the increasing of $Q$.

Similarly, when $F < 1$, the duration of half switching cycle is changed to $\pi/F > \pi$. OST BCB still exists in tiny $Q$, and the former stage B disappears first with the increasing of $Q$, and the OST is changed to CB [see Fig. 4(f)]. When $V_m(\theta)$ reaches $-1$ before $\theta = \pi/F$, the OST is changed to CBA [see Fig. 4(g)]. If the initial slope of $I_r(\theta)$ is greater than that of $I_m(\theta)$, stage B disappears and the OST is changed to CA [see Fig. 4(h)]. In summary, the OSTs when $F < 1$ and $D = 1$ are BCB, CB, CBA, and CA with the increasing of $Q$.

### B. OSTS IN PSM

In PSM, $F$ is fixed to unity and the possible OSTs are C-FED, BC-FE, and BCB-E. Typical waveforms of these OSTs are depicted in Fig. 5.

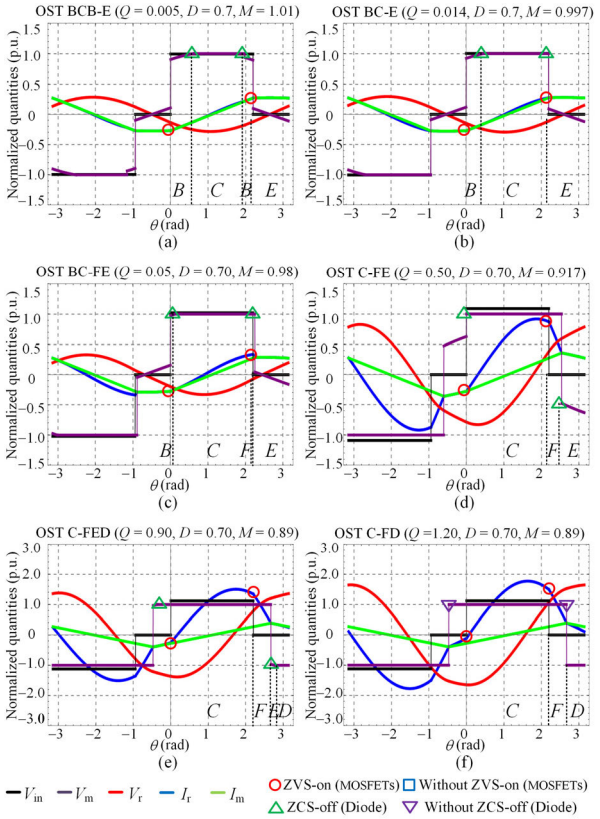


**FIGURE 5.** Typical waveforms in PSM. (a) OST BCB-E ($Q = 0.005$, $D = 0.7$, $M = 1.01$). (b) OST BC-E ($Q = 0.014$, $D = 0.7$, $M = 0.997$). (c) OST BC-FE ($Q = 0.05$, $D = 0.7$, $M = 0.98$). (d) OST C-FE ($Q = 0.5$, $D = 0.7$, $M = 0.917$). (e) OST C-FED ($Q = 0.90$, $D = 0.7$, $M = 0.89$). (f) OST C-FD ($Q = 1.2$, $D = 0.7$, $M = 0.89$).

When $Q$ is tiny, the OST is BCB-E [see Fig. 5(a)]. The latter stage B disappears first with the increasing of $Q$, and the OST is changed to BC-E [see Fig. 5(b)]. With slightly increasing $Q$ and the OST will change to BC-FE [see Fig. 5(c)]. Note that the transition from stage C to stage E is prohibited, and OST BC-E is just the boundary OST of OST BC-E and BC-FE [see Fig. 7(c)]. If $V_{mE}(\theta)$ cannot reach $-1$ when $\theta = \pi$, the OST is C-FE [see Fig. 5(d)]. If $V_{mE}(\theta)$ reaches $-1$ before $\theta = \pi$, the OST is C-FED [see Fig. 5(e)]. If the initial slope of $I_r(\theta)$ is greater than that of $I_m(\theta)$ at the end of stage F, the OST is C-FD [see Fig. 5(f)]. In summary, the OSTs in PSM are BCB-E, BC-E, BC-FE, C-FE, C-FED, and C-FD with the increasing of $Q$.

### C. OSTS IN ZERO LOAD CONDITIONS

When the load decreases to zero, there is $Q = 0$ and the available stages are B and E. The typical waveforms in OST B, and B-E are depicted in Fig. 6.

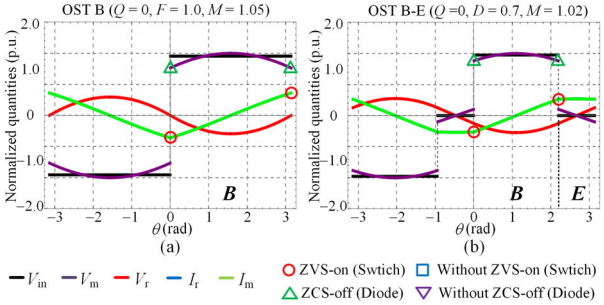


**FIGURE 6.** Typical waveforms in zero load condition. (a) OST B ($Q = 0$, $F = 1.0$, $M = 1.05$). (b) OST B-E ($Q = 0$, $D = 0.7$, $M = 1.02$).

As for OST B, $V_{\mathrm{mB}}(\theta)$ is given as

$$V_{\mathrm{mB}}(\theta) = \frac{m-1}{mM}\left(\cos\left(\frac{\theta}{\sqrt{m}}\right) - \cot\left(\frac{\pi}{2F\sqrt{m}}\right)\sin\left(\frac{\theta}{\sqrt{m}}\right)\right). \tag{11}$$

In order to maintain stage B, $\max|V_{\mathrm{mB}}(\theta)|$ should not exceed 1, and the zero load voltage gain $M_{\text{zero-load}}$ is given as

$$M_{\text{Zero-Load}} = \frac{m-1}{m}\sec\left(\frac{\pi}{2\sqrt{m}F}\right). \tag{12}$$

It can be noted from (12) that when $F$ approaches $F_{\mathrm{m}}$, $M_{\text{zero-load}}$ approaches infinity. Hence, zero load is not allowed when $F$ is close to $F_{\mathrm{m}}$. OST B-E is with solving a transcendental equation and no analytical expression for $M$ can be given.

### D. OST DISTRIBUTION OF LLC

The OST distribution map of *LLC* when $m = 5$ with PFM and PSM are depicted in Fig. 7.

In Fig. 7, the critical operation points are the intersections of multiple OSTs, which are denoted as the red dots. In Fig. 7 (a), OSTs CA, CBA, CB, and AC coverage at $Q = Q_1$, while OSTs CB, BCB, ABC, BC, and AC coverage at $Q = Q_0$. Similarly, in Fig. 7(c), OSTs C-FD, C-FED, and C-FE coverage at $Q = Q_2$, while OSTs BCB-E, BC-E, and BC-FE coverage at $Q = Q_0$. The expressions of $Q_0$, $Q_1$, and $Q_2$ are given as

$$Q_0 = \frac{\pi}{4(m-1)}, Q_1 = \frac{(2m-1)\pi}{4(m-1)}, Q_2 = \frac{m\pi}{4(m-1)}. \tag{13}$$

When *LLC* is with PFM, $M$ can be greater or smaller than 1 mainly related to $F$. The OST distribution is separated by $F = 1$ when $Q > Q_0$. By continuously increasing $Q$ or decreasing $F$, the OSTs are BCB, CB, CBA, and CA when $F < 1$ and the OSTs are BCB, BC, ABC, and AC when $F > 1$. BCB exists in all $F$ range when $Q$ is relatively small. In zero load condition, $Q = 0$ and the OST is changed to B. When $F = 1$ and $Q > Q_0$, $M$ is always 1, which is independent of load. $M$ shrinks in the same OST when $Q$ increases. When *LLC* is with PSM, $M$ is smaller than 1 when $Q$ is not too small. By continuously increasing $Q$ or decreasing $D$, the OSTs are BCB-E, BC-E, BC-FE, C-FE, C-FED, and C-FD. As for OSTs BCB-E, BC-E, and BC-FE, the corresponding $Q$ is small and the output voltage regulation capability is weak. C-FE is with a wide $Q$ and $M$ variation range. No matter in PFM or PSM, the $M$-$F$, $Q$-$F$, $M$-$D$, $Q$-$D$ distribution maps show a reverse relation of $Q$ and $M$.

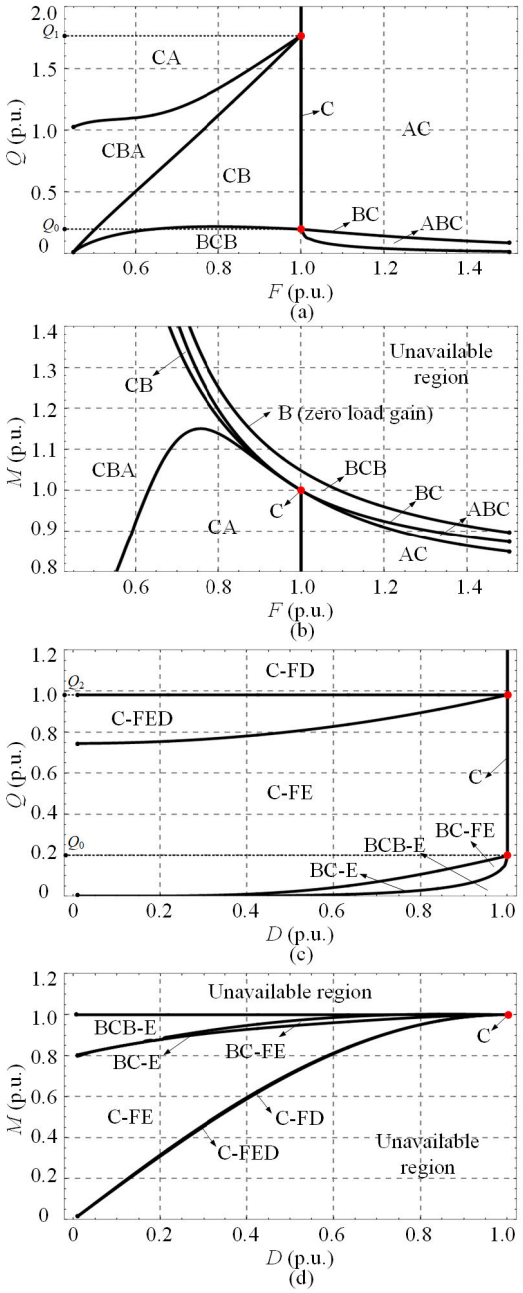


**FIGURE 7.** OST distribution map of *LLC* when $m = 5$. (a) $Q - F$ distribution with PFM. (b) $M - F$ distribution with PFM. (c) $Q - D$ distribution with PSM. (d) $M - D$ distribution with PSM.

## IV. STEADY-STATE PARAMETER CALCULATION OF LLC

The operation of *LLC* is determined once $Q$, $F$, and $D$ are given. Hence, steady-state parameters such as $I_{\mathrm{RMS}}$, $I_{\mathrm{mRMS}}$, $I_{\mathrm{Peak}}$, $V_{\mathrm{Peak}}$, $M_{\mathrm{Peak}}$, ZVS-on, and ZCS-off regions can be

obtained. $I_{\mathrm{RMS}}$, $I_{\mathrm{mRMS}}$ are related to the conduction loss of *LLC*, $V_{\mathrm{Peak}}$ determines the choice of resonant capacitors, $M_{\mathrm{Peak}}$ is related to the design of the transformer ratio, and ZVS-on and ZCS-off regions are related to the switching loss of devices.

### A. IRMS AND CONDUCTION LOSS ANALYSIS

Normalized $I_{\mathrm{RMS}}$ and $I_{\mathrm{mRMS}}$ are given as

$$I_{\mathrm{RMS}} = \sqrt{\frac{F}{\pi}\sum\int_0^{\theta_{\mathrm{X}}} I_{\mathrm{rX}}^2(\theta)d\theta}, I_{\mathrm{mRMS}} = \sqrt{\frac{F}{\pi}\sum\int_0^{\theta_{\mathrm{X}}} I_{\mathrm{mX}}^2(\theta)d\theta}. \tag{14}$$

With (14), the conduction loss of *LLC* can be estimated and compared in different control methods.

### B. PEAK VOLTAGE GAIN AND REGION ANALYSIS

In PFM, the constraint condition of the ZVS-on boundary condition is also the boundary condition of $M_{\mathrm{Peak}}$, which can be obtained by setting the initial resonant current to zero [15], [37]. Adding this condition to the OST boundary equations, and the boundary of CBA/CA can be solved. The result shows that the boundary of CBA/CA across the zero initial resonant current line. The crossing frequency $F_{\mathrm{i}}$ can be solved by the transcendental equation given as

$$\tan\left(\frac{\pi}{F_i}\right) = \frac{4\pi(m-1)F_i}{4F_i^2(2m-1)+\pi^2}. \tag{15}$$

$F_{\mathrm{i}}$ decreases monotonously with the increasing of $m$. When $m$ approaches infinity, the minimum of $F_{\mathrm{i}}$ is 0.735. When $m = 1$, the maximum of $F_{\mathrm{i}}$ is 1. Therefore, $M_{\mathrm{Peak}}$ occurs in OST CBA when $F_{\mathrm{m}} < F < F_{\mathrm{i}}$ while it occurs in OST CA when $F_{\mathrm{i}} < F < 1$ [37]. In PSM, $M$ decreases monotonously with the decreasing of $D$ and the increasing of $Q$. Hence, $M_{\mathrm{Peak}}$ appears in zero load when $D = 1$, which can be calculated by (12). The ZVS-on boundary can be obtained with a similar approach, the boundary of C-FED/C-FD across the initial resonant current line. The crossing duty ratio $D_{\mathrm{i}}$ is given as

$$\begin{cases} D_{\mathrm{i}} = 1 - \dfrac{2}{\pi}\arctan\left(\dfrac{\pi}{2}\right) \approx 0.361 \\ M_{\mathrm{i}} = \dfrac{2}{\sqrt{\pi^2+4}} \approx 0.537 \end{cases}. \tag{16}$$

The ZVS-on curves in the OST distribution map is depicted in Fig. 8.

To achieve ZVS-on for MOSFETs, $F$ or $D$ should not be too small when $Q$ is high. To achieve ZCS-off for diodes, stage B or E should be included in the OST.

### C. CPEAK RESONANT VOLTAGE ANALYSIS

The power stored in the resonant tank can be classified into the power stored in $L_{\mathrm{r}}$ and the power stored in $C_{\mathrm{r}}$. In one switching cycle, these two parts exchange power with each other. Therefore, $V_{\mathrm{Peak}}$ is reached when $I_{\mathrm{r}}(\theta) = 0$. From the ZVS-on region analysis above, whether $I_{\mathrm{r}}(\theta) = 0$ occurs

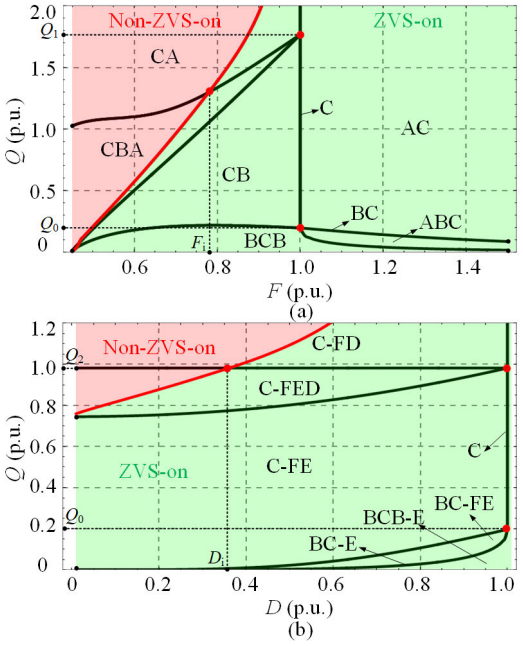


**FIGURE 8.** ZVS-on distribution map of *LLC* when $m = 5$. (a) ZVS-on distribution with PFM. (b) ZVS-on distribution with PSM.

before or after the switching of primary switches depends on the operation region. In ZVS region, $I_{\mathrm{r}}(\theta)$ across zero in stage C, and $V_{\mathrm{Peak}}$ is the amplitude of resonant voltage in stage C. In non-ZVS-on region, $I_{\mathrm{r}}(\theta)$ across zero in stage A or stage D, and $V_{\mathrm{Peak}}$ is the amplitude of resonant voltage in stage A or stage D.

As for OST C, $V_{\mathrm{Peak\text{-}C}}$ is given as

$$V_{\mathrm{Peak\text{-}C}} = \sqrt{\frac{16Q^2}{\pi^2} + \frac{\pi^2}{4(m-1)^2}}. \tag{17}$$

As for OST AC, $V_{\mathrm{Peak\text{-}AC}}$ is given as

$$V_{\mathrm{Peak\text{-}AC}} = 1 - \frac{1}{M} + \sqrt{\frac{\pi^2}{4F^2(m-1)^2} + \left(1 - \frac{1}{M} - \frac{4Q}{\pi F}\right)^2}. \tag{18}$$

As for OST CA, $V_{\mathrm{Peak\text{-}CA}}$ is given as

$$V_{\mathrm{Peak-CA}} = \begin{cases} 1 - \frac{1}{M} + \sqrt{\frac{\pi^2}{4F^2(m-1)^2} + \left(1 - \frac{1}{M} + \frac{4Q}{\pi F}\right)^2}, \\ \text{ZVS-on} \\ 1 + \frac{1}{M} + \sqrt{\frac{\pi^2}{4F^2(m-1)^2} + \left(1 + \frac{1}{M} - \frac{4Q}{\pi F}\right)^2}, \\ \text{Non-ZVS-on} \end{cases}. \tag{19}$$

As for other OSTs, there are no closed-form expressions.

### D. PEAK RESONANT CURRENT ANALYSIS

$I_{\mathrm{Peak}}$ is related to the current stress of MOSFETs, and $I_{\mathrm{Peak}}$ occurs when $V_{\mathrm{r}}(\theta) = 0$. When $Q$ is small, $I_{\mathrm{Peak}}$ may occur in stage B and stage E. When $Q$ is large, $I_{\mathrm{Peak}}$ occurs in stage C

or stage F. Two examples of $I_{\mathrm{Peak}}$ in OST C-FE are depicted in Fig. 9. In Fig. 9, whether $I_{\mathrm{Peak}}$ occurs in stage C or stage F is determined by two angles, $\varphi$, and $\theta_{\mathrm{C}}$, where $\varphi$ is with the peak value of $I_{\mathrm{r}}(\theta)$ in stage C and $\theta_{\mathrm{C}} = D\pi$. Hence, $I_{\mathrm{Peak}}$ is given as

$$I_{\mathrm{Peak}} = \begin{cases} \sqrt{\left(\dfrac{1}{M} - 1 - V_{\mathrm{rC}}(0)\right)^2 + (I_{\mathrm{rC}}(0))^2}, \varphi \le D\pi \\ I_{\mathrm{rC}}(D\pi), \varphi > D\pi \end{cases}$$
$$\varphi = \frac{\pi}{2} - \operatorname{acr\,tan}\left(\frac{MI_{\mathrm{rC}}(0)}{1 - M - MV_{\mathrm{rC}}(0)}\right). \tag{20}$$

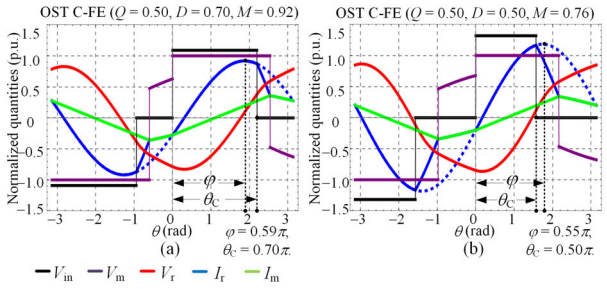


**FIGURE 9.** (a) OST C-FE ($Q = 0.50$, $D = 0.70$, $M = 0.92$), $\varphi < \theta_{\mathrm{C}}$. (b) OST C-FE ($Q = 0.50$, $D = 0.50$, $M = 0.76$), $\varphi > \theta_{\mathrm{C}}$.

## V. OSTS AND OPTIMIZATION OF LLC WITH 2DOFS

### A. OST DISTRIBUTION OF LLC WITH 2DOFS

If 2DOFs are considered simultaneously, the possible OSTs increases rapidly. The OSTs when $F > 1$ are ABC-F, AC-F, C-FD, C-FED, C-FE, BC-FE, and BCB-E. The OSTs when $F < 1$ are CA-D, CBA-D, CB-D, CB-ED, CB-E, BCB-E, C-FD, C-FED, C-FE, and BC-FE. The 3D distribution of OSTs when $F > 1$ and $F < 1$ are depicted in Fig. 10.

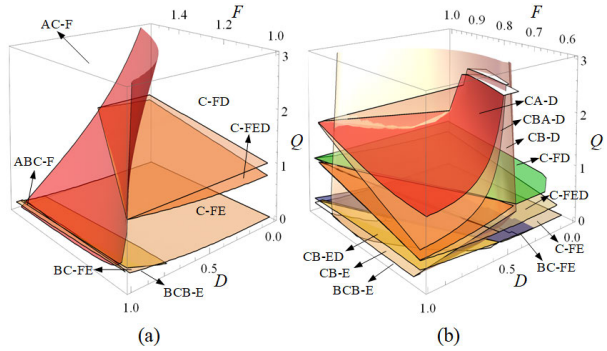


**FIGURE 10.** 3D distribution of OSTs. (a) When $F > 1$. (b) When $F < 1$.

### B. OPTIMIZATION OF LLC WITH 2DOFS

When *LLC* is operating at a given working point (usually $Q$ and $M$ are given), there is one equality constraint of the 2DOFs already included in the OST equations (power balance equation). Hence, there exists infinite combinations of $F$ and $D$. Denote the control coordinate, optimization objective, and constraint conditions as $\mathbf{X} = (F, D)$, $\boldsymbol{A}(\mathbf{X})$, and $\boldsymbol{B}(\mathbf{X})$. Typical $\boldsymbol{A}(\mathbf{X})$ can be $I_{\mathrm{RMS}}$, $I_{\mathrm{mRMS}}$, $I_{\mathrm{Peak}}$, and $V_{\mathrm{Peak}}$. The constraint conditions $\boldsymbol{B}(\mathbf{X})$ is classified into three types. 1) Convergence of the nonlinear transcendental OST equations. 2) Positive duration of each stage. 3) Satisfaction of every stage conditions.

Generally speaking, when $\mathbf{X}$ is away from (1, 1), the performance of *LLC* deteriorates. When $F < 1$, a smaller $D$ requires a lower $F$, which will make $\mathbf{X}$ farther from (1, 1). Hence, $D = 1$ is the optimization result when $F < 1$, which indicates that PFM is the best solution when $F < 1$. When $F > 1$, the reduction of $M$ can be realized by increasing $F$ and reducing $D$. Denote the control coordinate with PFM and PSM as $(F_{\max}, 1)$ and $(1, D_{\min})$, the optimal control coordinate $\mathbf{X_{opt}} = (F_{\mathrm{opt}}, D_{\mathrm{opt}})$ exists with $1 < F_{\mathrm{opt}} < F_{\max}$, $D_{\min} < D_{\mathrm{opt}} < 1$. Because the nonlinear transcendental OST equations are probably non-convex, regular convex optimization method may converge to local optima. Hence, a numerical calculation of optimal control coordinate $\mathbf{X_{opt}}$ is proposed, and the procedure is depicted in Fig. 11.

The procedure contains control coordinate table $\boldsymbol{C}(\mathbf{X})$, the optimization objective $\boldsymbol{A}(\mathbf{X})$, the constraint conditions $\boldsymbol{B}(\mathbf{X})$, the predefined range of $M$, $Q$, and the iteration steps (d$M$, d$Q$), and (d$F$, d$D$). $\boldsymbol{C}(\mathbf{X})$ is a four dimensional numerical table ($M$, $Q$, $F_{\mathrm{opt}}$, $D_{\mathrm{opt}}$) to store the optimal control coordinate with different $M$ and $Q$. $\boldsymbol{A}(\mathbf{X})$ can be designed arbitrarily as long as it is continuous. The predefined range of $M$ and $Q$ can be set to optimize within a certain range of $M$ and $Q$. The iteration step (d$M$, d$Q$), and (d$F$, d$D$) determine the accuracy of the distribution of optimal control coordinate.

The procedure contains two loops. The iteration variables in the outer loop are $M$ and $Q$. As for a given $M$ and $Q$, the control coordinate with PFM and PSM can be calculated to determine the upper bound of $F$ ($F_{\max}$) and lower bound of $D$ ($D_{\min}$). The inner loops are divided into 7 OST loops (ABC-F, AC-F, C-FD, C-FED, C-FE, BC-FE, and BCB-E), and the inputs of the OST loops are $M$, $Q$, $F_{\max}$, and $D_{\min}$. Take OST AC-F loop as an example, with the four input variables, the OST equations can be solved to find whether the control coordinate $\mathbf{X_{AC-F}}$ exists. If $\mathbf{X_{AC-F}}$ doesn't exist, the corresponding exit flag ($\mathrm{EF_{AC\text{-}F}}$) is reset ($\mathrm{EF_{AC\text{-}F}} = 0$) and if $\mathbf{X_{AC-F}}$ exists, $\mathbf{X_{AC-F}}$ is preserved. After one iteration of the inner loop, $M$ and $Q$ are increased by iteration step d$M$ and d$Q$ to start a new iteration in the inner loop. After the inner loop traverses all possible control coordinate in OST AC-F loop, it outputs the control coordinate $\mathbf{X_{opt(AC-F)}}$ with minimum $\boldsymbol{A}(\mathbf{X_{AC-F}})$. After the inner loops for all OSTs are finished, the optimal control coordinate $\mathbf{X_{opt}}$ for a certain $M$ and $Q$ can be found by selecting the minimum of the outputs of the OST loops. Add $\mathbf{X_{opt}}$ to $\boldsymbol{C}(\mathbf{X})$ and start a new iteration with $M = M+$ d$M$ and $Q = Q+$ d$Q$ until $M$ and $Q$ traverse the predefined range of $M$ and $Q$ and the four dimensional numerical table $\boldsymbol{C}(\mathbf{X})$ is generated.

When $\boldsymbol{A}(\mathbf{X}) = I_{\mathrm{RMS}}$, d$M = 0.1$, d$Q = 0.025$, d$F = 0.025$, d$D = 0.025$, and the predefined range of $M$ and $Q$ are given as

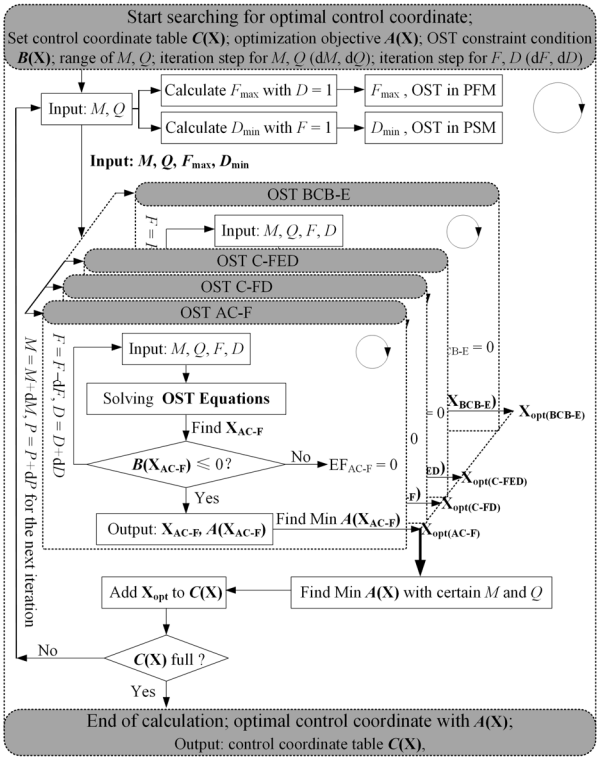


**FIGURE 11.** Procedure to determine the optimal control coordinates.

$M \in [0.5, 0.9]$, $Q \in [0, 1]$, the control coordinate trajectories are depicted in Fig. 12. The frequency limit $F_{\text{lim}}$ is chosen as 1.525 for practical consideration.

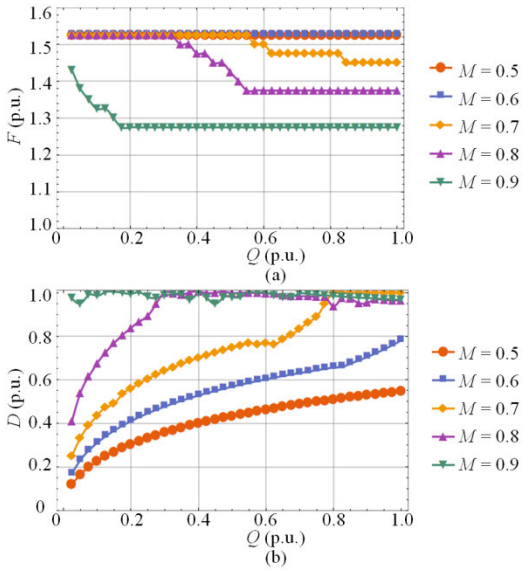


**FIGURE 12.** The control coordinate trajectories with minimum $I_{\text{RMS}}$. (a) Optimal frequency $F$. (b) Optimal duty ratio $D$.

In low $Q$ condition, there is $F_{\text{opt}} = F_{\text{lim}}$. A higher $F_{\text{lim}}$ corresponds to a higher $F_{\text{opt}}$ and a lower $D_{\text{opt}}$. When $M = 0.5$ and 0.6, there is $F_{\text{opt}} = F_{\text{lim}}$ in all $Q$ range. When $M$ is closer to unity, $F_{\text{opt}}$ is no longer $F_{\text{lim}}$ with the increasing of $Q$. With the increasing of $Q$, the OSTs with minimum $I_{\text{RMS}}$ are BCB-E, BC-FE, C-FE, C-FED, C-FD, and AC-F. Although the trajectory of optimal control is not smooth in some of the operation points, it can be fitted into a smooth and monotonic curve for feedback consideration by replacing the non-monotonic operation points with the monotonic sub-optimal operation points. The ZVS-on boundary occurs in OSTs C-FED, and C-FD, which can be calculated by adding an extra equation of $I_{\text{rC}}(0) = 0$ to the OST equations. The ZCS-off boundary can be obtained by the boundaries of OSTs ABC-F/AC-F, C-FE/AC-F, and C-FED/C-FD.

The ZVS-on and ZCS-off implementation of minimum $I_{\text{RMS}}$ are depicted in the 3D control coordinate trajectories in Fig. 13. In Fig. 13(a), the red curve is the ZVS-on boundary curve. All the control coordinate trajectories when $M = 0.5$, 0.6, 0.7, 0.8, and 0.9 are with ZVS-on implementation. The green curve in Fig. 13(b) is the ZCS-off boundary curve, in low $Q$ condition, the OSTs are BCB-E, BC-FE, C-FE, and C-FED. These OSTs are with ZCS-off due to stage E. In medium and high $Q$ condition, the OSTs are C-FD or AC-F, and ZVS-off cannot be achieved.

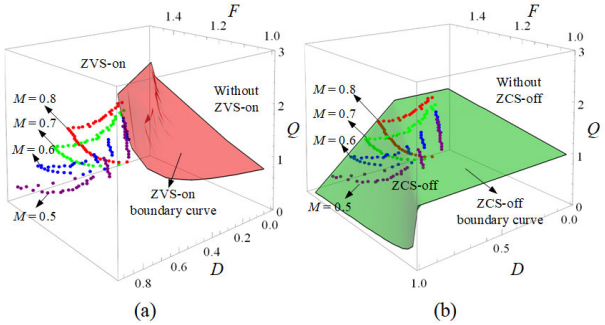


**FIGURE 13.** 3D control coordinate trajectories with minimum $I_{\text{RMS}}$. (a) ZVS-on implementation. (b) ZCS-off implementation.

The comparison of $I_{\text{RMS}}$ with $\boldsymbol{A}(\mathbf{X}) = I_{\text{RMS}}$, PFM, and PSM are depicted in Fig. 14, where the $y$-axis is $\sigma(I_{\text{RMS}})\%$, which is defined as

$$\sigma(I_{\text{RMS}})\% = \frac{I_{\text{RMS}} - \text{Min}(I_{\text{RMS}})}{\text{Min}(I_{\text{RMS}})} \times 100\%. \tag{21}$$

where $\text{Min}(I_{\text{RMS}})$ is the $I_{\text{RMS}}$ value when $\boldsymbol{A}(\mathbf{X}) = I_{\text{RMS}}$.

In PFM, $\sigma(I_{\text{RMS}})\%$ is negative in low $Q$ conditions when $M = 0.5$, 0.6, and 0.7. This is because $F$ in PFM is far beyond $F_{\text{lim}}$ to achieve a low $M$ (e.g. there is $F = 11.9$ when $M = 0.5$, $Q = 0.1$, which is impossible practically). When $M = 0.7$, $Q > 0.75$, $M = 0.8$, $Q > 0.35$, and $M = 0.9$, there is $F < F_{\text{lim}}$ and $\sigma(I_{\text{RMS}})\% > 0$. In high $Q$ conditions, $\sigma(I_{\text{RMS}})\%$ is around 15%−20%, which indicates that PFM is with 15%−20% higher $I_{\text{RMS}}$ in an identical $M$ and $Q$ condition. In PSM, there is $\sigma(I_{\text{RMS}})\% > 0$ when $Q$ is not too low ($Q > 0.1$). In high $Q$ conditions, $\sigma(I_{\text{RMS}})\%$ is around 30%. When $M$ approaches unity, $\sigma(I_{\text{RMS}})\%$ is getting smaller. When $\boldsymbol{A}(\mathbf{X}) = V_{\text{Peak}}$, the control coordinate trajectories are depicted in Fig. 15,

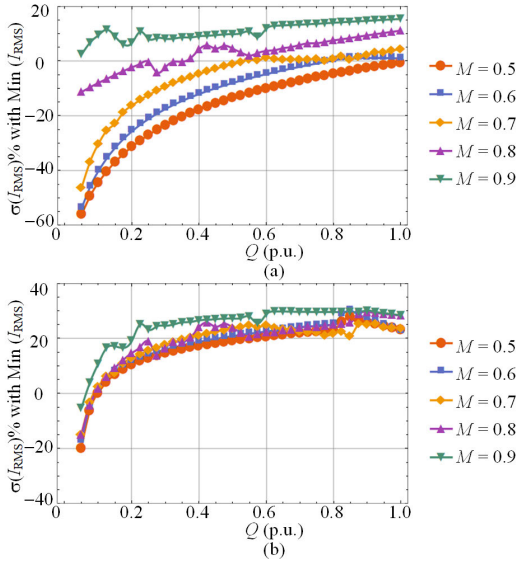


**FIGURE 14.** Comparison of $I_{RMS}$. (a) $\sigma(I_{RMS})$% with PFM and minimum $I_{RMS}$. (b) $\sigma(I_{RMS})$% with PSM and minimum $I_{RMS}$.

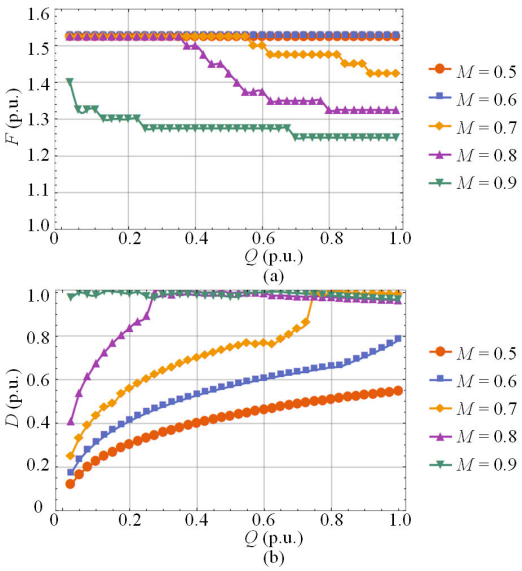


**FIGURE 15.** The control coordinate trajectories with minimum $V_{Peak}$. (a) Optimal frequency $F$. (b) Optimal duty ratio $D$.

which is very similar to the control coordinate trajectories with minimum $I_{RMS}$.

Similarly, the definition of $\sigma(V_{Peak})\%$ is given in (22), and the comparison of $V_{Peak}$ with $\boldsymbol{A}(\mathbf{X}) = V_{Peak}$, PFM, and PSM are depicted in Fig. 16.

$$\sigma(V_{Peak})\% = \frac{V_{Peak} - \mathrm{Min}(V_{Peak})}{\mathrm{Min}(V_{Peak})} \times 100\%. \tag{22}$$

where $\mathrm{Min}(V_{Peak})$ is the $V_{Peak}$ value with $\boldsymbol{A}(\mathbf{X}) = V_{Peak}$.

In Fig. 16, $\sigma(V_{Peak})\%$ is around 10% in PFM, and it is 30%−80% in PSM in high $Q$ conditions. Similar results can be obtained when other single or combinations of electric quantities are selected as $\boldsymbol{A}$ $(\mathbf{X})$. Fig. 14 to Fig. 16 proved

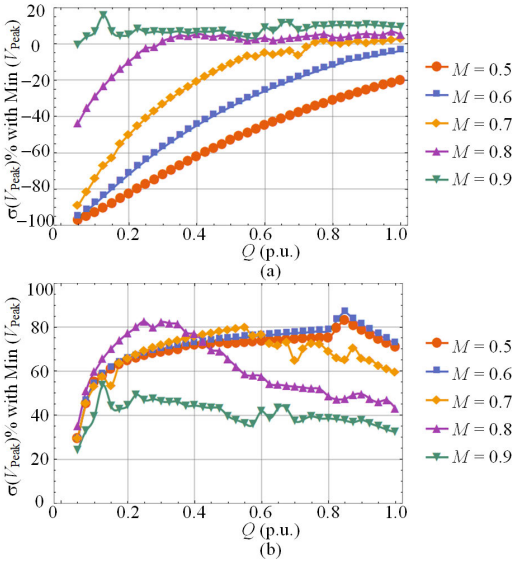


**FIGURE 16.** Comparison of $V_{Peak}$. (a) $\sigma(V_{Peak})$% with PFM and minimum $V_{Peak}$. (b) $\sigma(V_{Peak})$% with PSM and minimum $V_{Peak}$.

the effectiveness of the numerical optimal control coordinate calculation procedure and the conclusions can be drawn:

1) PFM and PSM are not the optimal solutions in buck mode ($M < 1$) from the perspective of $I_{RMS}$, $I_{mRMS}$, $I_{Peak}$, and $V_{Peak}$. To achieve a small $M$ in low $Q$ conditions, $F$ in PFM has to be very high, and $D$ is PSM has to be very tiny.

2) When $M$ is close to unity or $Q$ is very high, the optimal control coordinate is very close to PFM.

3) Both PFM and proposed optimal control coordinate are always with ZVS-on implementation while PSM in high $Q$ conditions may lose ZVS-on implementation.

4) Lower $M$ or $Q$ is beneficial to the ZCS-off implementation of the proposed optimal control coordinate. ZCS-off implementation cannot be achieved with PFM and it is almost irrelevant to $M$ or $Q$ in PSM when $Q < 0.85$.

## VI. EXPERIMENTAL RESULT

Two HB *LLC* converter prototypes are built to verify the feasibility and to demonstrate the advantages of the proposed 2DOFs optimization. The prototype is depicted in Fig. 17, and the parameters are listed below.

1) Primary side
   a) DC capacitor: 22$\mu$F/1.5kV, MKP capacitor, paralleled with 10nF and 100nF CBB capacitor.
   b) MOSFETs: CREE C2M0080170P × 2.
2) Secondary side
   a) DC capacitor: 22$\mu$F/1.5kV MKP capacitor, paralleled with 10nF and 100nF CBB capacitor.
   b) Diodes: CREE C5D25170H × 4.
3) Resonant tank
   a) Resonant capacitor: 47 × 9 + 33 × 6 = 621nF, MMKP capacitor;
   b) Resonant inductor: 2.86$\mu$H/2.81$\mu$H;
   c) Magnetizing inductor: 500$\mu$H/522$\mu$H;

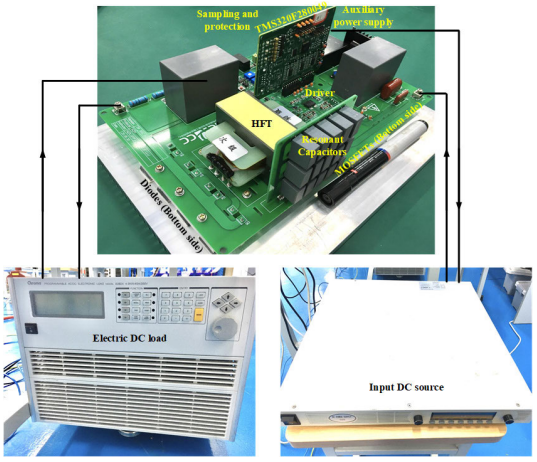


**FIGURE 17.** The prototype of the HB *LLC* resonant converter.

4) HFT: turn ratio: 1:2, Material: PC95/EEP70B.
5) Input voltage: 300V; Output voltage: 250V-350V.
6) Switching frequency: 75-150kHz.
7) Controller: DSP TMS320F280049.

The selection of the HB LLC topology is because it only needs two MOSFETs, and the input and output voltages are designed according to the project requirement. It has to be noted that the differences of resonant inductor and magnetizing inductor are brought by the HFT deviation. Although with parameter deviations, the resonant waveforms of the two converters under identical operation conditions are almost identical.

The output power range of the HB *LLC* converter prototype is from zero load to 500W. Moreover, the full output voltage regulation capability is from 10% load to full load. Control methods like PFM in [23]–[26], PSM in [28]–[30], and the proposed 2DOFs optimization are tested and compared. The switching frequency $f_s$ and duty ratio $D$ for the proposed 2DOFs optimization are calculated offline and pre-stored in the memory of the digital controller in practical operation.

### A. OPERATION WAVEFORMS

Rated condition ($V_{in} = 300$ V, $V_{out} = 300$ V), minimum gain condition $M_{min}$ ($V_{in} = 300$ V, $V_{out} = 250$ V), and maximum gain condition $M_{max}$ ($V_{in} = 300$ V, $V_{out} = 350$ V) with the three control method are tested and the comparison results are depicted from Fig. 18 to Fig. 22.

In Fig. 18, the three control methods are both with resonant frequency and maximum duty ratio (the dead time $t_d$ is set as $t_d = 1.2\mu$s in this case). The blue line denotes the input voltage of the HFT $v_{ab}$, the green line denotes resonant current $i_r$, which is piecewise sinusoidal in half and full load conditions, and the purple line denotes the resonant voltage $v_r$, which is also sinusoidal. In zero load condition, $i_r$ is triangular and the current sag is caused by $t_d$.

Fig. 19 shows the waveforms with $M_{min}$ condition with 10% load condition. In Fig. 19, $D$ has to be very tiny for PSM and the $f_s$ is higher than 170 kHz in PFM. In these

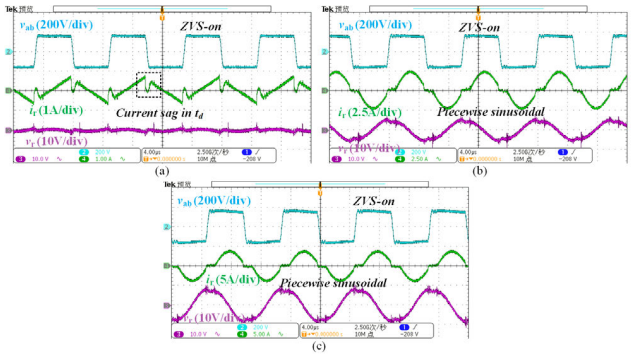


**FIGURE 18.** Operation waveforms with rated condition. (a) Zero load condition. (b) Half load condition. (c) Full load condition. (Ch2: HFT input voltage $v_{ab}$ with 200V/div, CH3: resonant voltage $v_r$ with 10V/div, Ch4: resonant current $i_r$ with 1A/2.5A/5A/div, time scale: 4$\mu$s/div).

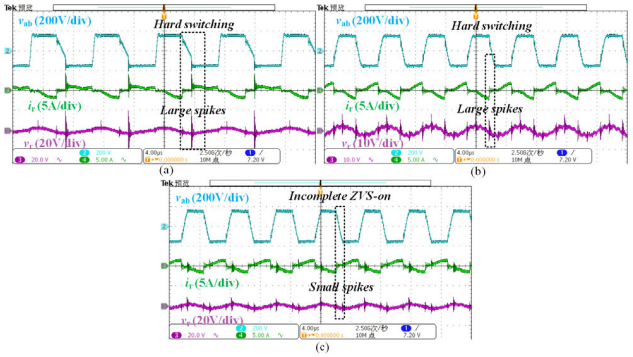


**FIGURE 19.** Operation waveforms with $M_{min}$ condition with 10% load condition. (a) PSM. (b) PFM. (c) 2DOFs optimization. (Ch2: HFT input voltage $v_{ab}$ with 200V/div, Ch3: resonant voltage $v_r$ with 10V/div, Ch4: resonant current $i_r$ with 5A/div, time scale: 4$\mu$s/div).

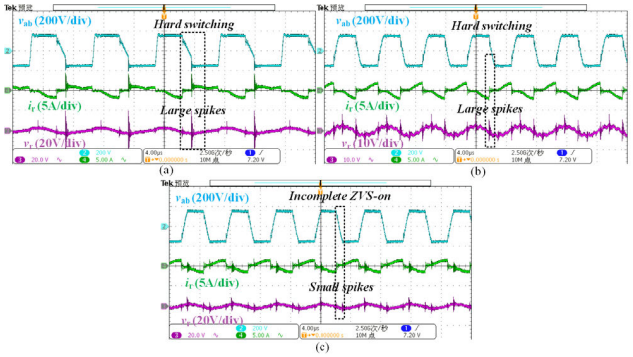


**FIGURE 20.** Operation waveforms with $M_{min}$ condition with half load condition. (a) PSM. (b) PFM. (c) 2DOFs optimization. (Ch2: HFT input voltage $v_{ab}$ with 200V/div, Ch3: resonant voltage $v_r$ with 20V/div, Ch4: resonant current $i_r$ with 5A/div, time scale: 4$\mu$s/div).

two conditions, ZVS-on characteristic is lost, which will cause very high current spike duration the turning on of MOSFETs and trigger the overcurrent protection. As for 2DOFs optimization, $f_s$ is chosen as 150 kHz (limited by the predefined maximum switching frequency), and the spikes are much smaller. Fig. 20 and Fig. 21 show the waveforms with $M_{min}$ condition with half load and full load conditions.

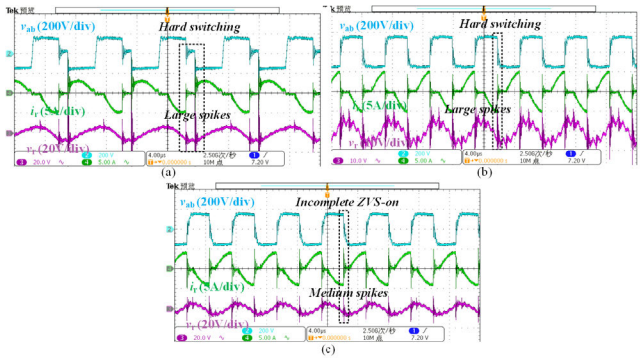


**FIGURE 21.** Operation waveforms ith $M_{min}$ condition with full load condition. (a) PSM. (b) PFM. (c) 2DOFs optimization. (Ch2: HFT input voltage $v_{ab}$ with 200V/div, Ch3: resonant voltage $v_r$ with 20V/div, Ch4: resonant current $i_r$ with 5A/div, time scale: 4$\mu$s/div).

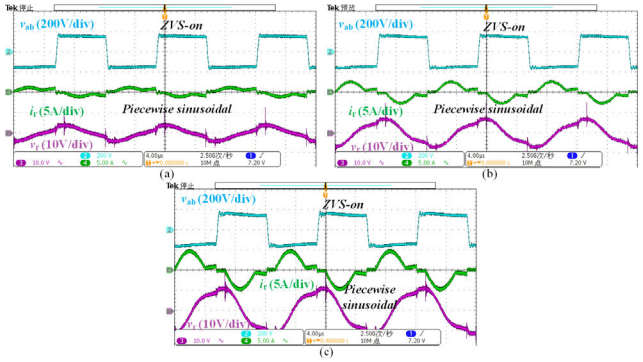


**FIGURE 22.** Operation waveforms with $M_{max}$ condition. (a) 10% load condition. (b) Half load condition. (c) Full load condition. (Ch2: HFT input voltage $v_{ab}$ with 200V/div, Ch3: resonant voltage $v_r$ with 20V/div, Ch4: resonant current $i_r$ with 5A/div, time scale: 4$\mu$s/div).

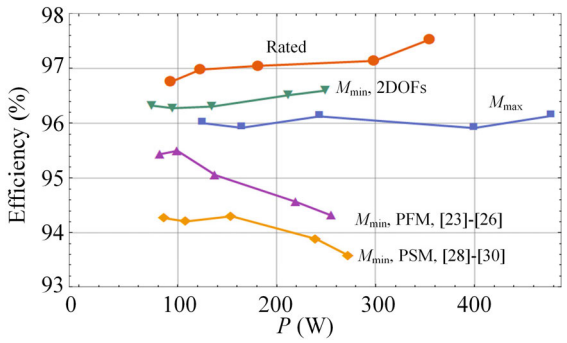


**FIGURE 23.** Experimental curves in different conditions.

Compared to 2DOFs optimization, both PSM and PFM are with large spikes and relatively high losses. The major reason the current and voltage spikes from Fig. 19 to Fig. 21 is the incomplete ZVS-on caused by high switching frequency. A higher switching frequency reduces the switching period as well as the initial resonant current to charge and discharge the parasitic capacitors of the MOSFETs during $t_d$. In $M_{max}$ condition depicted in Fig. 22, PSM is unavailable, PFM and the 2DOFs optimization are with the same control coordinate. The OSTs in 10% load condition is BCB and it becomes OST CB with the increase of power.

### B. THE EFFICIENCY CURVES WITH DIFFERENT CONTROL METHOD

The efficiency curves with the three control methods with three conditions are depicted in Fig. 23. The red, yellow, purple, green, and blue lines denote the rated condition, $M_{min}$ condition with PFM [23]–[26] /PSM [28]–[30] /2DOFs optimization, and the $M_{max}$ condition depicted from Fig. 18 to Fig. 22. Peak efficiency is achieved at the rated condition with 97.5%. In the comparison of $M_{min}$ condition, the efficiency of 2DOFs optimization is higher than PFM and PSM. As for $M_{max}$ condition, the efficiency is lower than the rated condition due to higher $I_{RMS}$ and $V_{Peak}$ caused by low switching frequency.

## VII. CONCLUSION

This paper gives a unified time domain OST analysis for *LLC* resonant converter with 2DOFs optimization (including switching frequency $f_s$, and duty ratio $D$). All possible operation modes of *LLC* resonant converter with 2DOFs are found and analyzed. On this basis, a general optimization method of *LLC* resonant converter with 2DOFs is proposed and the optimization objective can be designed arbitrarily. Compared with conventional control methods like PFM and PSM, the proposed 2DOFs optimization method is with lower $I_{RMS}$, $V_{Peak}$, higher efficiency, wider ZVS-on and ZCS-off region, and narrow switching frequency regulation range.

## APPENDIX

Steady state equations in stage C to stage F are as follows:

$$\begin{cases} I_{rC}(\theta) = \left(\dfrac{1}{M} - 1 - V_{rC}(0)\right)\sin(\theta) + I_{rC}(0)\cos(\theta) \\ I_{mC}(\theta) = I_{mC}(0) + \dfrac{\theta}{m-1} \\ V_{rC}(\theta) = \dfrac{1}{M} - 1 - \left(\dfrac{1}{M} - 1 - V_{rC}(0)\right) \\ \cos(\theta) + I_{rC}(0)\sin(\theta) \\ V_{mC}(\theta) = 1 \end{cases} \tag{A.1}$$

$$\begin{cases} I_{rD}(\theta) = (1 - V_{rD}(0))\sin(\theta) + I_{rD}(0)\cos(\theta) \\ I_{mD}(\theta) = I_{mD}(0) - \dfrac{\theta}{m-1} \\ V_{rD}(\theta) = 1 - (1 - V_{rD}(0))\cos(\theta) + I_{rD}(0)\sin(\theta) \\ V_{mD}(\theta) = -1 \end{cases} \tag{A.2}$$

$$\begin{cases} I_{rE}(\theta) = I_{mE}(\theta) = -\dfrac{\sqrt{m}}{m}V_{rE}(0)\sin\left(\dfrac{\theta}{\sqrt{m}}\right) \\ +I_{rE}(0)\cos\left(\dfrac{\theta}{\sqrt{m}}\right) \\ V_{rE}(\theta) = V_{rE}(0)\cos\left(\dfrac{\theta}{\sqrt{m}}\right) \\ +\sqrt{m}I_{rE}(0)\sin\left(\dfrac{\theta}{\sqrt{m}}\right) \\ V_{mE}(\theta) = -\dfrac{m-1}{m}V_{rE}(0)\cos\left(\dfrac{\theta}{\sqrt{m}}\right) \\ -\dfrac{m-1}{\sqrt{m}}I_{rE}(0)\sin\left(\dfrac{\theta}{\sqrt{m}}\right) \end{cases} \tag{A.3}$$

**TABLE 1. Detailed stage transition conditions.**

| From / To | Stage A | Stage B | Stage C |
|---|---|---|---|
| Stage A | - | $V_{mB}(\theta_B)$=-1 | $I_{mC}(\theta_C)=I_{rC}(\theta_C)$ |
| Stage B | $I_{mA}(\theta_A)=I_{rA}(\theta_A)$ | - | $I_{mC}(\theta_C)=I_{rC}(\theta_C)$ |
| Stage C | $I_{mA}(\theta_A)=I_{rA}(\theta_A)$ | $V_{mB}(\theta_B)$=1 | - |
| Stage D | $\Sigma\theta+\theta_A=D\pi$ | $\Sigma\theta+\theta_B=D\pi$ | $\Sigma\theta+\theta_C=D\pi$ |
| Stage E | $\Sigma\theta+\theta_A=D\pi$ | - | $\Sigma\theta+\theta_C=D\pi$ |
| Stage F | $\Sigma\theta+\theta_A=D\pi$ | $\Sigma\theta+\theta_B=D\pi$ | $\Sigma\theta+\theta_C=D\pi$ |
| From / To | Stage D | Stage E | Stage F |
| Stage A | - | - | - |
| Stage B | - | - | - |
| Stage C | - | - | - |
| Stage D | - | $V_{mE}(\theta_E)$=-1 | $I_{mF}(\theta_F)=I_{rF}(\theta_F)$ |
| Stage E | $I_{mD}(\theta_D)=I_{rD}(\theta_D)$ | - | $I_{mF}(\theta_F)=I_{rF}(\theta_F)$ |
| Stage F | $I_{mD}(\theta_D)=I_{rD}(\theta_D)$ | $V_{mE}(\theta_E)$=1 | - |

$$\begin{cases} I_{rF}(\theta) = -(1+V_{rF}(0))\sin(\theta) + I_{rF}(0)\cos(\theta) \\ I_{mF}(\theta) = I_{mF}(0) + \dfrac{\theta}{m-1} \\ V_{rF}(\theta) = -1 + (1+V_{rF}(0))\cos(\theta) + I_{rF}(0)\sin(\theta) \\ V_{mF}(\theta) = 1 \end{cases} \tag{A.4}$$

The detailed stage transition conditions are summarized in Table. 1.

## REFERENCES


[1] M. H. Ahmed, C. Fei, F. C. Lee, and Q. Li, "48-V voltage regulator module with PCB winding matrix transformer for future data centers," *IEEE Trans. Ind. Electron.*, vol. 64, no. 12, pp. 9302–9310, Dec. 2017.

[2] M. Mu and F. C. Lee, "Design and optimization of a 380–12 V high-frequency, high-current LLC converter with GaN devices and planar matrix transformers," *IEEE J. Emerg. Sel. Topics Power Electron.*, vol. 4, no. 3, pp. 854–862, Sep. 2016.

[3] Y. Hayashi, H. Toyoda, T. Ise, and A. Matsumoto, "Contactless DC connector based on GaN LLC converter for next-generation data centers," *IEEE Trans. Ind. Appl.*, vol. 51, no. 4, pp. 3244–3253, Jul. 2015.

[4] C. Fei, F. C. Lee, and Q. Li, "High-efficiency high-power-density LLC converter with an integrated planar matrix transformer for high-output current applications," *IEEE Trans. Ind. Electron.*, vol. 64, no. 11, pp. 9072–9082, Nov. 2017.

[5] J.-W. Kim, J.-P. Moon, and G.-W. Moon, "Duty-ratio-control-aided LLC converter for current balancing of two-channel LED driver," *IEEE Trans. Ind. Electron.*, vol. 64, no. 2, pp. 1178–1184, Feb. 2017.

[6] W. Feng, F. C. Lee, and P. Mattavelli, "Optimal trajectory control of LLC resonant converters for LED PWM dimming," *IEEE Trans. Power Electron.*, vol. 29, no. 2, pp. 979–987, Feb. 2014.

[7] Y. Wang, Y. Guan, K. Ren, W. Wang, and D. Xu, "A single-stage LED driver based on BCM boost circuit and *LLC* converter for street lighting system," *IEEE Trans. Ind. Electron.*, vol. 62, no. 9, pp. 5446–5457, Sep. 2015.

[8] F. Musavi, M. Craciun, D. S. Gautam, W. Eberle, and W. G. Dunford, "An LLC resonant DC–DC converter for wide output voltage range battery charging applications," *IEEE Trans. Power Electron.*, vol. 28, no. 12, pp. 5437–5445, Dec. 2013.

[9] J. Deng, S. Li, S. Hu, C. C. Mi, and R. Ma, "Design methodology of LLC resonant converters for electric vehicle battery chargers," *IEEE Trans. Veh. Technol.*, vol. 63, no. 4, pp. 1581–1592, May 2014.

[10] H. Haga and F. Kurokawa, "Modulation method of a full-bridge three-level LLC resonant converter for battery charger of electrical vehicles," *IEEE Trans. Power Electron.*, vol. 32, no. 4, pp. 2498–2507, Apr. 2017.

[11] D. Fu, Y. Liu, F. C. Lee, and M. Xu, "A novel driving scheme for synchronous rectifiers in LLC resonant converters," *IEEE Trans. Power Electron.*, vol. 24, no. 5, pp. 1321–1329, May 2009.

[12] X. Sun, Y. Shen, Y. Zhu, and X. Guo, "Interleaved boost-integrated LLC resonant converter with fixed-frequency PWM control for renewable energy generation applications," *IEEE Trans. Power Electron.*, vol. 30, no. 8, pp. 4312–4326, Aug. 2015.

[13] S. M. Tayebi, H. Hu, S. Abdel-Rahman, and I. Batarseh, "Dual-input single-resonant tank LLC converter with phase shift control for PV applications," *IEEE Trans. Ind. Appl.*, vol. 55, no. 2, pp. 1729–1739, Mar. 2019.

[14] B. Yang, "Topology investigation for front end DC/DC power conversion for distributed power system," Ph.D. dissertation, Dept. Elect. Comput. Eng., Virginia Polytech. Inst. Stage Univ., Blacksburg, VA, USA, 2003.

[15] B. Yang, F. C. Lee, A. J. Zhang, and G. Huang, "LLC resonant converter for front end DC/DC conversion," in *Proc. 17th Annu. IEEE Appl. Power Electron. Conf. Expo. (APEC)*, vol. 2, Mar. 2002, pp. 1108–1112.

[16] L. Bing, L. Wenduo, L. Yan, F. C. Lee, and J. D. van Wyk, "Optimal design methodology for LLC resonant converter," in *Proc. IEEE Appl. Power Electron. Conf.*, Mar. 2006, pp. 1–6.

[17] R. Beiranvand, B. Rashidian, M. R. Zolghadri, and S. M. H. Alavi, "Optimizing the normalized dead-time and maximum switching frequency of a wide-adjustable-range LLC resonant converter," *IEEE Trans. Power Electron.*, vol. 26, no. 2, pp. 462–472, Feb. 2011.

[18] C. Adragna, S. De Simone, and C. Spini, "A design methodology for LLC resonant converters based on inspection of resonant tank currents.," in *Proc. 23rd Annu. IEEE Appl. Power Electron. Conf. Expo.*, Feb. 2008, pp. 1361–1367.

[19] W. Feng and F. C. Lee, "Optimal trajectory control of LLC resonant converters for soft start-up," *IEEE Trans. Power Electron.*, vol. 29, no. 3, pp. 1461–1468, Mar. 2014.

[20] C. Fei, F. C. Lee, and Q. Li, "Digital implementation of soft start-up and short-circuit protection for high-frequency LLC converters with optimal trajectory control (OTC)," *IEEE Trans. Power Electron.*, vol. 32, no. 10, pp. 8008–8017, Oct. 2017.

[21] W. Feng, F. C. Lee, and P. Mattavelli, "Optimal trajectory control of burst mode for LLC resonant converter," *IEEE Trans. Power Electron.*, vol. 28, no. 1, pp. 457–466, Jan. 2013.

[22] C. Fei, Q. Li, and F. C. Lee, "Digital implementation of light-load efficiency improvement for high-frequency LLC converters with simplified optimal trajectory control," *IEEE J. Emerg. Sel. Topics Power Electron.*, vol. 6, no. 4, pp. 1850–1859, Dec. 2018.

[23] R. Beiranvand, B. Rashidian, M. R. Zolghadri, and S. M. H. Alavi, "Using LLC resonant converter for designing wide-range voltage source," *IEEE Trans. Ind. Electron.*, vol. 58, no. 5, pp. 1746–1756, May 2011.

[24] Z. Fang, T. Cai, S. Duan, and C. Chen, "Optimal design methodology for LLC resonant converter in battery charging applications based on time-weighted average efficiency," *IEEE Trans. Power Electron.*, vol. 30, no. 10, pp. 5469–5483, Oct. 2015.

[25] X. Fang, H. Hu, F. Chen, U. Somani, E. Auadisian, J. Shen, and I. Batarseh, "Efficiency-oriented optimal design of the LLC resonant converter based on peak gain placement," *IEEE Trans. Power Electron.*, vol. 28, no. 5, pp. 2285–2296, May 2013.

[26] R. Yu, G. K. Y. Ho, B. M. H. Pong, B. W.-K. Ling, and J. Lam, "Computer-aided design and optimization of high-efficiency LLC series resonant converter," *IEEE Trans. Power Electron.*, vol. 27, no. 7, pp. 3243–3256, Jul. 2012.

[27] H. Wang and Z. Li, "A PWM LLC type resonant converter adapted to wide output range in PEV charging applications," *IEEE Trans. Power Electron.*, vol. 33, no. 5, pp. 3791–3801, May 2018.

[28] B. McDonald and F. Wang, "LLC performance enhancements with frequency and phase shift modulation control," in *Proc. IEEE Appl. Power Electron. Conf. Expo. (APEC)*, Mar. 2014, pp. 2036–2040.

[29] M. Yu, D. Sha, and X. Liao, "Hybrid phase shifted full bridge and LLC half bridge DC–DC converter for low-voltage and high-current output applications," *IET Power Electron.*, vol. 7, no. 7, pp. 1832–1840, Jul. 2014.

[30] J. Kim, C. Kim, J. Kim, J. Lee, and G. Moon, "Analysis on load-adaptive phase-shift control for high efficiency full-bridge LLC resonant converter under light-load conditions," *IEEE Trans. Power Electron.*, vol. 31, no. 7, pp. 4942–4955, Jul. 2016.

[31] U. Mumtahina and P. J. Wolfs, "Multimode optimization of the phase-shifted LLC series resonant converter," *IEEE Trans. Power Electron.*, vol. 33, no. 12, pp. 10478–10489, Dec. 2018.

[32] D. Yang, C. Chen, S. Duan, J. Cai, and L. Xiao, "A variable duty cycle soft startup strategy for LLC series resonant converter based on optimal current-limiting curve," *IEEE Trans. Power Electron.*, vol. 31, no. 11, pp. 7996–8006, Nov. 2016.

[33] S. De Simone, C. Adragna, C. Spini, and G. Gattavari, "Design-oriented steady-state analysis of LLC resonant converters based on FHA," in *Proc. Int. Symp. Power Electron., Electr. Drives, Automat. Motion (SPEEDAM)*, May 2006, pp. 200–207.

[34] Y. Wei, Q. Luo, S. Chen, P. Sun, and N. Altin, "Comparison among different analysis methodologies for LLC resonant converter," *IET Power Electron.*, vol. 12, no. 9, pp. 2236–2244, Aug. 2019.
[35] C. Oeder, A. Bucher, J. Stahl, and T. Duerbaum, "A comparison of different design methods for the multiresonant LLC converter with capacitive output filter," in *Proc. IEEE 12th Workshop Control Model. Power Electron. (COMPEL)*, Jun. 2010, pp. 1–7.
[36] G. Ivensky, S. Bronshtein, and A. Abramovitz, "Approximate analysis of resonant LLC DC-DC converter," *IEEE Trans. Power Electron.*, vol. 26, no. 11, pp. 3274–3284, Nov. 2011.
[37] X. Fang, H. Hu, Z. J. Shen, and I. Batarseh, "Operation mode analysis and peak gain approximation of the LLC resonant converter," *IEEE Trans. Power Electron.*, vol. 27, no. 4, pp. 1985–1995, Apr. 2012.
[38] W. Liu, B. Wang, W. Yao, Z. Lu, and X. Xu, "Steady-state analysis of the phase shift modulated LLC resonant converter," in *Proc. IEEE Energy Convers. Congr. Expo. (ECCE)*, Sep. 2016, pp. 1–5.
[39] Y. Shen, H. Wang, F. Blaabjerg, X. Sun, and X. Li, "Analytical model for LLC resonant converter with variable duty-cycle control," in *Proc. IEEE Energy Convers. Congr. Expo. (ECCE)*, Sep. 2016, pp. 1–7.

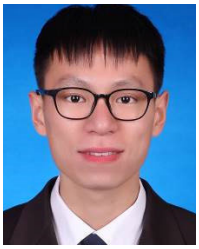

**ZIHENG XIAO** (Student Member, IEEE) was born in Zhejiang, China, in 1995. He received the B.S. degree in electrical engineering and automation, in 2017. He is currently pursuing the Ph.D. degree in electrical engineering with the College of Electrical and Information Engineering, Hunan University, Changsha.

His research interests include dual active bridge converters, resonant converters, and dc/dc converter series and parallel operation and modular converter systems.

**ZHIXING HE** (Member, IEEE) was born in Hunan, China, in 1989. He received the B.S. degree in information science and engineering from Central South University, Changsha, China, in 2011, and the Ph.D. degree in electrical engineering from Hunan University, Changsha, in 2017. He was a Postdoctoral Researcher with the Hunan University, from 2017 to 2018. He is currently an Associate Professor with the College of Electrical and Information Engineering, Hunan University. His research interests include power electronics, medium voltage dc systems, model predictive control, and modular multilevel converter.

**YONG NING** was born in Hunan, China, in 1980. He received the B.S., M.S., and Ph.D. degrees from Hunan University, Changsha, China, in 2003, 2010, and 2019, respectively. He is currently working as a Postdoctoral Researcher with Hunan University. His research interests include power electronics systems control and application, modeling and control of micro grid, and intelligence algorithm.

**HONGLIANG WANG** (Senior Member, IEEE) received the B.Sc. degree in electrical engineering from the Anhui University of Science and Technology, Huainan, China, in 2004, and the Ph.D. degree in electrical engineering from the Huazhong University of Science and Technology, Wuhan, China, in 2011.

From 2004 to 2005, he worked as an Electrical Engineer with Zhejiang Hengdian Thermal Power Plant. From 2011 to 2013, he worked as a Senior System Engineer with Sungrow Power Supply Company Ltd. From 2013 to 2018, he worked as a Postdoctoral Fellow with Queen's University. Since 2018, he has been with Hunan University, where he is currently a Full Professor with the College of Electrical and Information Engineering. He has authored over 60 technical articles in the journals and conferences. He is the inventor/co-inventor of 42 China issued patents, and eight U.S. issued patents. His current research interests include multilevel topology, high-gain topology, parallel technology and virtual synchronous generator (VSG) technology for photovoltaic application, and micro-grids application; and resonant converters and server power supplies, and LED drivers. He is also a Senior Member of China Electro-Technical Society (CES) and the China Power Supply Society (CPSS). He also serves as a member of CPSS Technical Committee on Standardization, a member of CPSS Technical Committee on Renewable Energy Power Conversion, a China Expert Group Member for IEC Standard TC8/PT 62786, the Vice-Chair for the IEEE Kingston Section, the Session Chair for ECCE 2015 and ECCE 2017, and a TPC Member for ICEMS 2012.

**AN LUO** (Senior Member, IEEE) was born in Changsha, China, in 1957. He received the B.S. and M.S. degrees in industrial automation from Hunan University, Changsha, in 1982 and 1986, respectively, and the Ph.D. degree in fluid power transmission and control from Zhejiang University, Hangzhou, China, in 1993.

From 1996 to 2002, he was a Professor with Central South University. Since 2003, he has been a Professor with the College of Electrical and Information Engineering, Hunan University, where he also serves as the Chief for the National Electric Power Conversion and Control Engineering Technology Research Center. His research interests include distributed generation, microgrid, and power quality. He was elected to the Chinese National Academy of Engineering (CNAE), in 2015, and the highest honor for scientists and engineers and scientists in China. He has won the highly prestigious China National Science and Technology awards three times, in 2014, 2010, and 2006.

**YANDONG CHEN** (Senior Member, IEEE) was born in Hunan, China, in 1979. He received the B.S. and M.S. degrees in instrument science and technology and the Ph.D. degree in electrical engineering from Hunan University, Changsha, China, in 2003, 2006, and 2014, respectively.

He is currently a Professor with the College of Electrical and Information Engineering, Hunan University. His research interests include power electronics for microgrid, distributed generation, power supply, and energy storage. He was a recipient of the 2014 National Technological Invention Award of China, and the 2014 WIPO-SIPO Award for Chinese Outstanding Patented Invention.

**JUNLING CHEN** received the B.Sc. degree in automation and the M.Sc. degree in control theory and control engineering from Central South University, Changsha, China, in 1999 and 2002, respectively, and the Ph.D. degree in electrical engineering from Tsinghua University, Beijing, China, in 2006.

He is currently a Research Fellow with Guangdong Zhicheng Champion Group Company Ltd., Dongguan, China. His research interests include power quality, active power filters, multilevel converters, medium voltage dc systems, and power amplifier.